Volume 1 | Number 1 | Jan 2013 | Pages 1–100

Journal of
Materials Chemistry A

Materials for energy and sustainability
www.rsc.org/materialsA

ROYAL SOCIETY OF CHEMISTRY

www.rsc.org/materialsA

ROYAL SOCIETY
OF CHEMISTRY

Journal Name

ARTICLE

One-Step Coating Inverted Polymer Solar Cells Using a Conjugated Polymer as Electron Extraction Additive[†]

Zuosheng Peng,[a] Yangdong Zhang,[a] Yuxin Xia,[a,c] Kang Xiong,[a] Chaosheng Cai,[a] Lianpeng Xia,[a]

Zhanhao Hu,[b] Kai Zhang,[b] Fei Huang,[*b] Lintao Hou[*a]

We report a facile technique of blending a conjugated polymer thieno[3,4-b]thiophene/benzodithiophene (PTB7):[6,6]-phenyl-C71-butyric acid methyl ester active materials with a conjugated interfacial modification polymer poly[(9,9-bis(3´-(N,N-dimethylamino) propyl)-2,7-fluorene)-alt-2,7-(9,9-dioctylfluorene)] (PFN) to simplify the coating process and improve the bulk heterojunction (BHJ) polymer solar cell (PSC) performance. The reason and result of the PFN self-organization via a spontaneous vertical delamination onto the ITO surface were investigated by charge transfer state, optical modelling based on transfer matrix formalism, surface energy measurement, scanning Kelvin probe force microscopy, impedance spectra analysis in conjunction with atomic force microscope and scanning electron microscope. The relaxed charge transfer state demonstrates that PFN doping has a negligible impact on the donor:acceptor heterojunction interface. The optical simulation of device structures indicates that doping PFN into BHJ has nearly no influence on the photon absorption profile of the active layer. Very encouraging device performance was achieved in the one-step coating PFN:BHJ PSC with ITO as the cathode, which is comparable to that of the two-step coating PSC. Moreover, for ITO-free inverted PSCs with PEDOT:PSS as the incident light top-electrode, decent device performance can also be obtained, demonstrating the remarkable universality through this facile strategy.

Introduction

Polymer solar cell (PSC), which has advantages of flexibility, light weight, portability, solution processing and low cost, is considered one of the promising solar energy conversion technologies in the future renewable energy systems. In recent years, power conversion efficiency (PCE) of PSCs has exceeded 10% within the laboratory, which nearly meets the requirements of commercialization.[1-6] The significant progress in PCE improvements is mainly attributed to designing and synthesizing new photoactive materials, creating novel architectures, controlling photoactive layer morphology and utilizing interface modification.[7-11] For high-performance devices, it was confirmed that the insertion of the nonconjugated or conjugated interfacial modification layer (IML) between the photoactive layer and the cathode is highly necessary, which facilitates charge collection and extraction by means of the work function modification and the interfacial charge redistribution.[12, 13] For example, nonconjugated polymers such as PEO, PEI and PEIE, etc., and conjugated polymers such as PFPA-1, FTBTF-N, and poly[(9,9-bis(3´-(N,N-dimethylamino) propyl)-2,7-fluorene)-alt-2,7-(9,9-

a Siyun Laboratory, Department of Physics, Jinan University, Guangzhou 510632, PR China. E-mail: thlt@jnu.edu.cn
b Institute of Polymer Optoelectronic Materials and Devices, State Key Laboratory of Luminescent Materials and Devices, South China University of Technology, Guangzhou 510640,China. E-mail: msfhuang@scut.edu.cn
c Biomolecular and Organic Electronics, IFM, and Center of Organic Electronics, Linköping University, SE-581 83 Linköping, Sweden.
† Electronic Supplementary Information (ESI) available. See DOI: 10.1039/x0xx00000x

Journal of Materials Chemistry A Accepted Manuscript

dioctylfluorene)] (PFN), etc., were used as IMLs to help collect and extract the negative charge carriers.[14-19] In 2015, Wu *et al.* proposed a highly efficient conjugated polymer PFN as the IML and achieved a certified PCE as high as 10.61%, which mainly attributes to the effect of an increased device built-in potential coming from the existence of interface dipole and an enhanced charge carrier mobility due to the reduced recombination loss.[3] The device lifetime can be greatly enhanced due to the better stability of interfacial materials to the water and oxygen in the air compared with the common low work function interfacial metals.[10, 16]

Although nonconjugated or conjugated polymers as IMLs can obviously improve the device performance, the addition of IMLs by solution coating certainly increases the fabrication complexity in the large area roll-to-roll processing due to the requirements of rigorous alignment of multiple layers, accurate thicknesses, limited mutual solubility, and so on.[5] For solving these problems, an easy spontaneous vertical phase separation technique was introduced in several studies. Wang *et al.* reported that doping a certain ratio nonconjugated polymer poly(vinylpyrrolidone) (PVP) into poly(3-hexylthiophene) (P3HT):[6,6]-phenyl-C61-butyric acid methyl ester (PCBM) bulk photoactive layer can lead to an enhancement of PCE about 13% due to the spontaneous vertical migration of PVP molecules to the surface of P3HT:PCBM active layer during the spin-coating processing.[20] Other nonconjugated polymers such as PEG, PDMS-*b*-PMMA, fullerene end-capped PEG and PEI were also mixed into the photoactive layer to form the interfacial buffer layer via self-assembly.[21-24] In addition, Zhang *et al.* reported a self-assembled BenMeIm-Cl ionic liquid as the cathode interfacial material.[25] However, it was reported that the stability of ionic-type materials in device is worse than their neutral part in device.[19] Although nonconjugated polymers as IMLs via self-organization have been reported by above several groups, conjugated interfacial polymers via a spontaneous vertical separation in nanocomposites have not yet been systematically investigated.

Conjugated interfacial polymers have many advantages compared to nonconjugated interfacial polymers. Firstly, the higher electrical conductivity of conjugated interfacial polymers, e.g. PFN, compared with insulating nonconjugated interfacial polymers, can make them be used as robust IMLs via self-assembly for high performance PSCs, especially when the interlayer thickness is more than 20 nm.[12, 26] It can be predicted that the doping concentration sensitivity to PCEs will be decreased for conjugated polymers due to the favorable conductive property. Secondly, it was reported that devices based on conjugated interfacial polymers exhibited the larger open circuit voltage than devices based on nonconjugated interlayer polymers, e.g., PEO and PEI, indicating that conjugated interfacial polymers can form lower energetic barriers for electrons.[27] Thus, the conjugated interfacial polymers exhibited much better device performance both in

organic light-emitting diodes and PSCs compared to nonconjugated interfacial polymers. Last but not the least, besides the highly polar side-chain groups, conjugated interfacial polymers with the unsaturated backbone chain structure can show a wide range of adaptability of different work-function cathodes, which work well for the very high work-function electrodes, e.g. Au, while nonconjugated interfacial polymers only work well for the relatively low work-function electrodes, e.g. Al, due to the saturated backbone chain structure.[25]

Recently, Lei *et al.* synthesized an amine-based fullerene derivative PCBDAN, which can play vital roles of electron acceptor and IML simultaneously.[28, 29] For clarifying the PCBDAN amino-functionalized fullerene derivative effect on the hole carrier extraction, Cai *et al.* proposed a hole trapping mechanism based on poly [N-9′-heptadecanyl-2, 7-carbazole-*alt*-5, 5-(4′, 7′-di-2-thienyl-2′, 1′, 3′-benzothiadiazole)] and P3HT donors by using femtosecond transient absorption spectroscopy measurements. They found that the hole trapping behavior depends on the relative energetic position of the hole transport states mostly determined by the highest occupied molecular orbital (HOMO) level of donors and the trapping states induced by the amine end groups, which provides important guidance for this strategy.[30]

Based on the above reports, we incorporate a small amount of versatile conjugated polymer PFN with terminal amino electron-donating groups into the bulk heterojunction (BHJ) mixture of a conjugated polymer thieno[3,4-b]thiophene/benzodithiophene (PTB7): [6,6]-phenyl-C71-butyric acid methyl ester (PCBM[70]) in chlorobenzene (CB):1, 8-diiodooctane (DIO) solution to reduce the work function of the ITO (or Al/TiO$_x$) and simplify the solar cell fabrication complexity. The HOMO level of PTB7 is ~ -5.15 eV, which is much higher than the ionization state of PFN amino group of ~ -5.40 eV, indicating the hole trapping by PFN amino group should be negligible.[10, 18] We demonstrate that PFN molecules can migrate vertically to the bottom of PTB7:PCBM[70] layer and form an IML between ITO and the photoactive layer based on the measurements of contact angle, surface energy, built-in potential, optical field distribution, morphology and charge transfer state, etc. The one-step coating device can achieve the comparable device performance to that of the conventional two-step coating cell. The strategy is also suitable to the attractive roll-to-roll compatible ITO-free inverted solar cells with Al/TiO$_x$ as the cathode and PEDOT:PSS as the top anode. This work provides not only the useful method for optimizing device structure but also new insights into the nature of the conjugated polymer as IMLs.

Results and discussion

The chemical structures of PTB7, PFN and PCBM[70] and the processing steps of two types of devices are shown in Fig. 1. For the two-step coating device with an inverted structure of
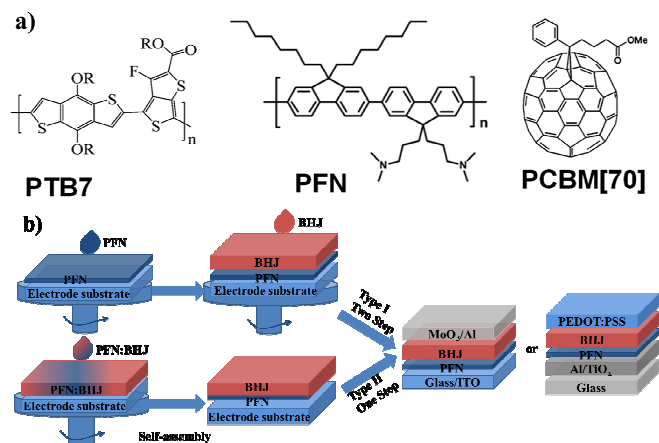
a)

PTB7   **PFN**   **PCBM[70]**

b)

Fig. 1 (a) Molecular structures of PTB7, PFN and PCBM[70]. (b) The inverted device structure and the fabrication process of Type I and Type II.

Fig. 2 (a) *J-V* and (b) dark *J-V* curves of Type I and Type II (0, 1, 3, 5 and 7 wt%) devices. (c) *J-V* curves of ITO-free inverted devices.

ITO/PFN/PTB7:PCBM[70](BHJ)/MoO$_3$/Al (Type I), conjugated polymer PFN interlayer was spin coated on top of ITO layer and then PTB7:PCBM[70] active layer was spin coated on top of the PFN interlayer. For the alternative one-step coating device with an inverted structure of ITO/PFN:PTB7:PCBM[70](PFN:BHJ)/MoO$_3$/Al (Type II), organic PFN:BHJ nanocomposite solution was directly spin coated on top of the ITO substrate with PFN layer formation via vertical self-assembly after drying.

The current density versus voltage (*J-V*) curves of Type I and Type II devices with variable PFN weight ratios (0, 1, 3, 5 and 7 wt%) are shown in the Fig. 2a. The conventional Type I device shows an average PCE of 7.50 %, an open-circuit voltage (*V*$_{oc}$) of 0.77 V, a short-circuit current density (*J*$_{sc}$) of 16.12 mA/cm^2 and a fill factor (FF) of 0.61. For comparison, the best Type II device performance is obtained with the optimum weight ratio of PFN to BHJ of 3 wt%, showing an average PCE of 7.07%, a *V*$_{oc}$ of 0.76 V, a *J*$_{sc}$ of 15.74 mA/cm^2 and a FF of 0.59, which are comparable to those of the conventional type I device. The detailed device parameters are shown in Table 1. With the increase of the weight ratio of PFN, the PCEs of the Type II
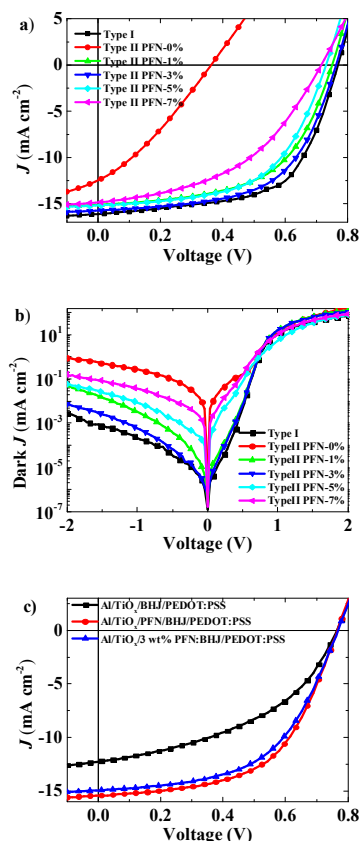
devices increase dramatically from 1.39% to 7.07% with the weight ratio of PFN doping into BHJ from 0 to 3 wt%, and then decrease from 6.21% to 4.90% with the weight ratio of PFN to BHJ from 5 wt% to 7 wt%. The device dark *J-V* curves are presented in Fig. 2b. It can be seen that the dark currents of Type II devices with weight ratios (0, 1, 5 and 7 wt%) are higher than that of the conventional Type I device, which can cause an increase in series resistance and a decrease in shunt

Table 1 Photovoltaic parameters of Type I and Type II devices with various PFN doping weight ratios (0, 1, 3, 5 and 7 wt%) under illumination of AM 1.5G (100 mW/cm^2). Over 20 devices were tested for each averaged value.

Type	Doping weight ratio of PFN (wt%)	J_{sc} (mA/cm^2)	V_{oc} (V)	FF	PCE$_{ave}$ [PCE$_{max}$] (%)
Type I	-	16.12	0.77	0.61	7.50[7.62]
Type II	0	12.47	0.36	0.31	1.39[1.65]
Type II	1	15.12	0.75	0.56	6.37[6.48]
Type II	3	15.74	0.76	0.59	7.07[7.14]
Type II	5	15.19	0.73	0.56	6.21[6.30]
Type II	7	14.85	0.72	0.46	4.90[5.12]

PCE$_{max}$: maximum power conversion efficiency; PCE$_{ave}$: average power conversion efficiency.

ARTICLE

Table 2 Performance of the ITO-free inverted devices with the structure of Al/TiO$_x$/BHJ/PEDOT:PSS, Al/TiO$_x$/PFN/BHJ/PEDOT:PSS and Al/TiO$_x$/3wt% PFN:BHJ/PEDOT:PSS measured under illumination of AM 1.5G (100 mW/cm^2). Over 20 devices were tested for each averaged value.

Device structure	J_{sc} (mA/cm^2)	V_{oc} (V)	FF	PCE$_{ave}$ [PCE$_{max}$] (%)
Al/TiO$_x$/BHJ/PEDOT:PSS	12.27	0.76	0.44	4.12 [4.32]
Al/TiO$_x$/PFN/BHJ/PEDOT:PSS	15.46	0.77	0.56	6.60 [6.78]
Al/TiO$_x$/3wt% PFN:BHJ/PEDOT:PSS	15.01	0.77	0.54	6.21 [6.41]

PCE$_{max}$: maximum power conversion efficiency; PCE$_{ave}$: average power conversion efficiency.

resistance. However, the Type II device with the PFN doping weight ratio of 3 wt% shows very low dark current and is comparable to that of the conventional Type I device. Considering the similar light and dark *J-V* characteristics of Type I and Type II (3 wt%) devices, we can speculate that the reason of the Type II device performance improvement originates in the spontaneous PFN vertical stratification via self-assembly from BHJ. The new PFN interlayer can be formed on top of the ITO surface to facilitate the electron extraction and collection. The lower PCE of Type II device (3 wt%) than that of Type I device (7.07% vs. 7.50%) may be due to the incomplete PFN-rich buried interlayer after drying, as seen from the corresponding difference in *V$_{oc}$* (0.76 V vs. 0.77 V). For 5% and 7% PFN:BHJ films, a slightly thick and porous PFN sub-layer would be formed between BHJ and ITO, leading to the lower device performance.[20] The lower *V$_{oc}$* is mainly attributed to the higher dark current for 5 wt% and 7 wt% Type II devices.

We also examine the universality of this approach by fabricating roll-to-roll compatible ITO-free inverted devices. As shown in Fig. 2c and Table 2, the device with an inverted structure of Al/TiO$_x$/BHJ/PEDOT:PSS obtains a poor PCE of 4.12%, while the device with an inverted structure of Al/TiO$_x$/PFN/BHJ/PEDOT:PSS achieves an improved PCE of 6.60% due to the insertion of PFN IML. Furthermore, when the optimal 3 wt% PFN is doped into BHJ with an inverted device structure of Al/TiO$_x$/PFN(3 wt%):BHJ/PEDOT:PSS, an average PCE of 6.21% is obtained, proving the adaptability of PFN doping BHJ method for other device structure systems. The lower PCE of ITO-free devices than that of ITO-based devices (6.21% vs. 7.07%) in the optimum weight ratio of PFN to BHJ of 3:97 should be mainly ascribed to the lower conductivity of the PEDOT:PSS layer than ITO as the transmittance spectra of the ITO and PEDOT:PSS films are similar in a wide wavelength range (Fig. S1). The accuracy of the *J$_{sc}$* is confirmed by the corresponding external quantum efficiency (EQE) measurement, as shown in Fig. S2. The calculated *J$_{sc}$* obtained from EQE curves of both ITO-based and ITO-free inverted devices are in good agreement with the values of *J$_{sc}$* measured by *J-V* characteristics.

The surface and bottom molecular distributions of the pristine BHJ and PFN:BHJ films were analysed by measuring their physicochemical property. As seen in Fig. 3a, the water droplet has the smallest contact angle of 79° on the spin-coated PFN film surface, whereas it shows 85°, 97° and 95° on the spin-coated hydrophobic PCBM[70], PTB7 and BHJ film

surfaces, respectively. The similar water contact angles of PTB7 and BHJ films indicate that the BHJ film surface is richer in PTB7. When 3 wt% PFN was doped into the BHJ, the water droplet contact angle nearly remains unchanged (95°), showing that a small amount of PFN molecules have little effect on the BHJ molecular surface distribution and PFN with polar functional groups may sink to the interior or bottom of the BHJ film during the spin coating process. It was believed that the vertical self-assembly is formed by differing surface energies in organic blends on the basis of the minimization of the total system energy.[24, 25, 31, 32] For exploring the PFN vertical self-organization, surface energies of PFN, PCBM[70], PTB7, BHJ and PFN(3 wt%):BHJ solid films prepared by spin coating were measured using water and formamide as the probe liquids based on Owens equation $\gamma_l(1+\cos\theta)=2(\gamma_s^D\gamma_l^D)^{1/2}+2(\gamma_s^P\gamma_l^P)^{1/2}$, where γ_s and γ_l are the surface energies of the sample and the probe liquid, and D and P refer to the dispersion and polar components of the surface energy, respectively (see details in Supporting Information).[33] As displayed in Fig. 3b, the high-surface energies of PFN (49.8 mN/m) and ITO (55 mN/m) indicate that PFN molecules in
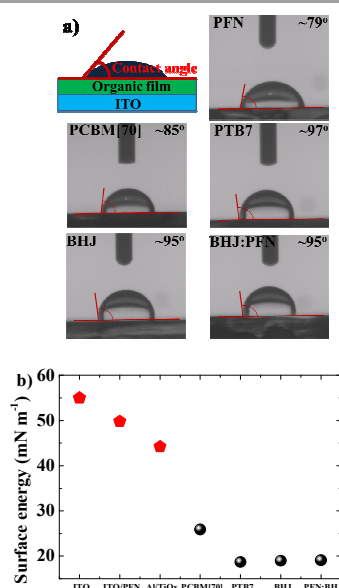

Fig. 3 (a) Photographs of water contact angle on top of the various films. (b) Surface energies of various films.

Journal Name

ARTICLE

PFN:BHJ solutions can migrate vertically towards the high-surface energy ITO to get a bulk free energy minimization and thus an ultrathin PFN layer can be formed thermodynamically between ITO and BHJ layer during the spin-coating process.[24] In other words, because PFN surface energy is substantially higher than BHJ, the buried ITO interface would be almost exclusively composed of PFN by means of interaction free energies of the film constituents after drying. It is important to note that the BHJ (19.1 mN/m) film has a similar low surface energy to the PFN:BHJ (19.0 mN/m) nanocomposite film, confirming that there is nearly no hydrophilic PFN molecule existing on the surface of the PFN:BHJ nanocomposite film. Also the surface energy of the pure PTB7 (18.7 mN/m) film is similar to that of BHJ or PFN:BHJ film, revealing that a PTB7-rich interface decorates the exposed surface of two kinds of active films, which is also consistent with their contact angle results. The above mentioned surface energy analysis also applies to ITO-free inverted devices, where the PFN molecules can migrate vertically towards high-surface energy Al/TiO$_x$ (44.2 mN/m) via self-assembly in the drying process.

The observation is further corroborated by scanning Kelvin probe force microscopy (SKPFM) measurements, while the work function modifications from 4.64 eV (ITO) to 4.06 eV (ITO/PFN),[10] 4.42 eV (ITO/PFN:BHJ) or 4.39 eV (ITO/PFN/BHJ) are obtained, confirming that the surface of PFN:BHJ nanocomposite film is very lack of PFN for attaining a thermodynamically air stable surface. However, due to the very weak signal intensity of nitrogen, we failed to map the PFN depth profile inside the active layer by energy-dispersive X-ray spectroscopy (EDS). The PFN distribution in bulk using charge transfer state probing method and scanning electron microscope (SEM) will be discussed in the next part.

The built-in potential of solar cells is accessible by means of the capacitive method. Fig. 4 depicts the impedance spectroscopy analysis of capacitance-voltage (C^{-2}-V) characteristics at 10 kHz in the dark.[34, 35] The built-in potential can be deduced from C^{-2}-V characteristic curve fitting with Mott-Schottky relation $C^{-2} = 2(V_{bi} - V)/(Ae\varepsilon\varepsilon_0 N_A)$, where V_{bi} is built-in potential, V is the applied voltage, A is the device effective area (14 mm^2), e corresponds to elementary charge, ε

is the relative dielectric constant (assuming ε of 3.5), ε_0 is the permittivity of the vacuum and N_A accounts for the concentration of acceptor impurities.[36] We can deduce the values of V_{bi} according to the voltage which is located at the maximal of capacitance (the flat-band condition).[37] In case Type II device without the PFN layer, V_{bi} of 0.31 ± 0.02 V is obtained, which is consistent to its low V_{oc}, implying the significant effect of PFN on the improvement of built-in electric field. When the PFN layer was inserted between the ITO and the BHJ layer, V_{bi} can increase to 0.66 ± 0.02 V for Type I device, while V_{bi} of 0.66 ± 0.02 V is obtained for Type II device (3 wt%), which is quite the same as that of the conventional Type I device. Obviously, doping PFN into BHJ blends can obtain the same effect on improving the built-in electric field as that of PFN/BHJ bilayer structure. In other words, the spontaneous PFN molecule sinking via self-assembly on the surface of ITO in the drying process is evidenced by the quite equal values of V_{bi} of Type I and Type II (3 wt%) devices.

Although PFN molecules can migrate into the ITO surface from the PFN:BHJ nanocomposite solution during the spin-coating process, it is not sure whether a few residual PFN molecules were distributed in the donor:acceptor interface. For a better understanding of PFN influence on the active layer property, charge transfer (CT) state of BHJ and PFN:BHJ nanocomposite films were implemented by detecting the electroluminescence (EL) emission and highly sensitive Fourier-transform photocurrent spectroscopy (FTPS) absorption spectra.[38, 39] It is believed that the EL peak corresponds to the donor:acceptor interface CT emission state. As the EL emission of pure PTB7 has a reported light-emitting peak around 820 nm and pure PCBM[70] has an emission at 720 nm,[17] it can be seen that 3 wt% PFN doping into the active layer does not change the CT emission of BHJ with a peak at ~ 1010 nm for both BHJ and PFN:BHJ nanocomposite films, as shown in Fig. 5a, indicating that there is no PFN molecule existing on the donor:acceptor interface. On the other hand, theoretical CT absorption energy state (E_{CT}) can be deduced from the external quantum efficiencies of the charge transfer states (EQE_{CT}).[40, 41]

$$EQE_{CT}(E) = \frac{f}{E\sqrt{4k\pi\lambda T}}exp(\frac{-(E_{CT} + \lambda - E)^2}{4k\pi\lambda T})$$

Where T is temperature, λ is the reorganization energy associated to charge transfer absorption, f is the prefactor and k is the Boltzmann constant. In Fig. 5b, the BHJ film shows E_{CT} value of 1.36 eV, which is exactly the same as 1.36 eV of PFN(3 wt%):BHJ nanocomposite film. The CT absorption results are consistent to the corresponding CT emission spectra, which are also in accordance with the same built-in potentials of Type I and Type II (3 wt%) devices. However, when the higher 7 wt% PFN dopes into the BHJ, the E_{CT} shifts about 10 meV to 1.37 eV, implying that excessive PFN molecules can involve in the donor:acceptor interface or the bulk interpenetrating network. This leads to the decrease of the device performance (Table 1). The energy shift (~ 10 meV) does not correspond to
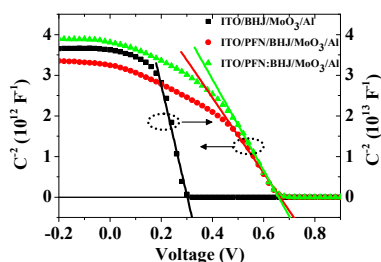

Fig. 4 Impedance spectroscopy analysis of C^{-2}-V characteristics of the inverted Type I and Type II (0 and 3 wt%) devices at 10 KHz in the dark.
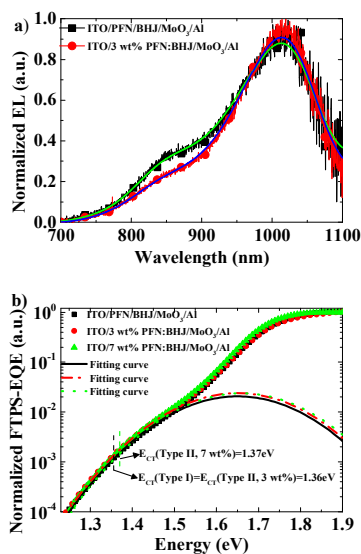
Fig. 5 (a) Normalized EL spectra of Type I and Type II (3 wt%) devices. (b) Normalized FTPS spectra of Type I and Type II (3, 7 wt%) devices with the theoretical FTPS-EQE fitting.

the difference in V_{oc} (~ -40 mV) between 3 wt% and 7 wt% PFN-doping Type II devices, indicating that the large leakage current is the unintended loss of the open-circuit voltage (Fig. 2b). We emphasize that the EL spectra of 3 wt% and 7wt% have little difference due to the weak detector signal intensity in the 1000-1100 nm wavelength range. In a word, the EL and FTPS results of Type I and Type II (3 wt%) devices demonstrate that the addition of a tiny amount of PFN into the BHJ does not influence the pristine donor:acceptor interface of the bulk active layer because of the spontaneous PFN vertical self-assembly.

To investigate the effect of the device configuration changes on the optical absorption profile, transfer matrix method is employed to model optical calculations.[9, 42] The spectral radiation of AM 1.5G (300 nm-1000 nm) and the experimentally measured refractive indices (n) and extinction coefficients (k) of the BHJ and PFN(3 wt%):BHJ absorber materials used in the simulations are presented in Fig. 6a. The photon absorption rate profiles can be derived based on above data, as shown in Fig. 6b and 6c. The absorbed photon flux density curves of two types of devices are very similar except the slightly higher power dissipation in the PFN interlayer for Type I device. The maximal photon flux density is 1.56×10^{28} m^{-3}s^{-1} and 1.52×10^{28} m^{-3}s^{-1} at 230 nm thickness relative to the substrate for Type I and Type II (3 wt%) devices, respectively, indicating that doping 3 wt% PFN into BHJ has negligible influence on the photon absorption of the active layer. The absorption spectra of PFN(3 wt%):BHJ and BHJ films are shown in Fig. S3. The similar absorption spectra imply that PFN material almost has no contribution to the harvesting of photons with vibronic features similar to the BHJ film. However, it should be noted that a little better interference
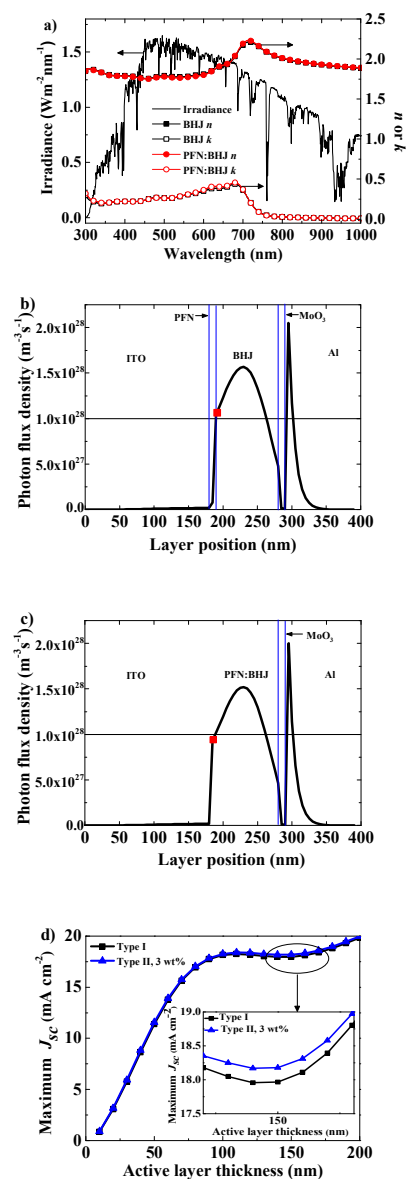

Fig. 6 (a) Spectral radiation of AM 1.5G (300nm-1000nm) and the measured refractive index (n) and extinction coefficient (k) of the BHJ and PFN(3 wt%):BHJ active layers. (b) Absorbed photon flux density of Type I cell with the structure of ITO(180 nm)/PFN(10 nm)/PTB7:PCBM[70](95 nm)/MoO$_3$(10 nm)/Al(100 nm) and (c) Type II cell with the configuration of ITO(180 nm)/PFN(3 wt%):PTB7:PCBM[70] (100 nm)/MoO$_3$(10 nm)/Al(100 nm), respectively. (d) Variation of corresponding maximum J_{sc} simulated through transfer matrix method with the variation of active layer thickness for two types of polymer solar cells under AM 1.5G illumination (100 mW/cm^2).

effect exists in Type I device compared to Type II device when we plot the optimal maximum photocurrent as function of the active layer thickness by neglecting any electrical losses and assuming that every photon absorbed in the active layer gives
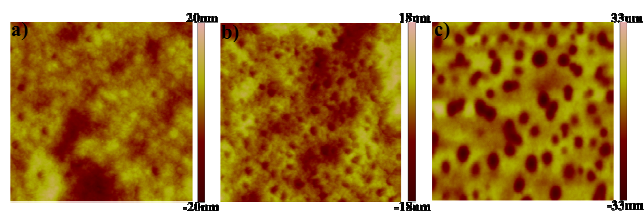
Fig. 7 AFM images of (a) PTB7:PCBM[70], (b) PFN(3 wt%):PTB7:PCBM[70] and (c) PFN(7 wt%):PTB7:PCBM[70] films (size= 5μm × 5μm).

rise to an electron in the outer circuit, as shown in Fig. 6d, illuminating that PFN mixing into BHJ blends is more suitable to roll-to-roll processing due to the photocurrent insensitivity to the active layer thickness variation.

As the large leakage current is related to the film morphology, the BHJ and PFN:BHJ films topographies were investigated by atomic force microscopy (AFM), as shown in Fig. 7. The root-mean-square (RMS) roughness values of BHJ, PFN(3 wt%):BHJ and PFN(7 wt%):BHJ films are 3.97 nm, 4.04 nm and 8.41nm, respectively. The comparable RMS values of BHJ and PFN(3 wt%):BHJ films indicate that adding a tiny amount (3 wt%) of PFN into BHJ almost has no impact on the film roughness. However, a honeycomb array of holes distributed in the PFN(3 wt%):BHJ film implies that PFN molecules might sink to the bottom of the BHJ layer during the spin-coating process and the vacant holes were produced after drying. This honeycomb structure has little effect on the film compactness, which can be seen from the good dark current curve in Fig. 2b. However, when a relatively large amount of PFN (7 wt%) were added into the BHJ, the size of honeycombs becomes bigger and the RMS value increases sharply. The uneven and non-compact film morphology is the key reason for the poor PFN(7 wt%):BHJ device dark current (Fig. 2b). This would be an interesting topic for further study.

The effect of PFN vertical migration to the ITO surface via self-assembly can be confirmed by SEM, as shown in Fig. 8. It is clear that the cross sectional SEM image of Type II device (ITO/PFN:BHJ/MoO$_3$/Al) is quite similar to that of the Type I device (ITO/PFN/BHJ/MoO$_3$/Al), confirming that PFN molecules are successfully migrated and stratified via self-assembly after drying. We emphasize that this SEM result is never reported in
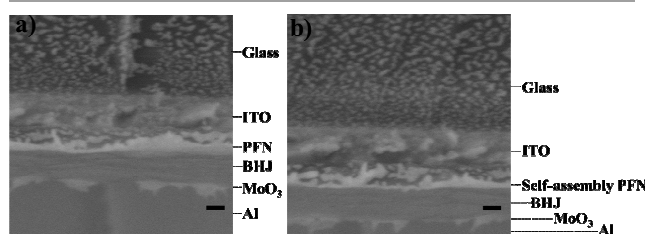
the previous studies.

Conclusions

In this work, efficient PSCs were successfully fabricated and simplified by doping the conjugated polymer PFN into the PTB7:PCBM[70] photoactive mixture. Vertical self-assembly stratification of conjugated PFN molecules can be formed after drying due to the strong interaction between PFN and ITO or PFN and TiO$_x$ with very high surface energies. Compared with those of the complicated two-step coating device, the built-in potential, optical field distribution and charge transfer state of the one-step coating device can still keep unaltered. Also the SEM images confirm the stratified structure of PFN:BHJ nanocomposite after drying. The PCE and J_{sc} values as high as 7.07% and 15.74 mA/cm^2 are obtained under the optimum 3 wt% PFN doping ratio, representing the highest device performance for interfacial conjugated polymer doping BHJ solar cells achieved to date. Moreover, for ITO-free inverted PSCs with a PEDOT:PSS layer as the top anode electrode, a decent PCE of 6.21 % is achieved, providing a new effective approach for the roll-to-roll compatible PSC fabrication process through this strategy.

Experimental section

Materials: PTB7 and PCBM[70] were purchased from 1-material Inc. and Solenne Inc., respectively. PEDOT:PSS (Clevious PH1000) solution was mixed with 5% dimethyl sulfoxide (DMSO) (Alfa Aesar 99.9%) and 0.5% surfactant (FS-30) for higher conductivity and better surface wettability. The PFN material was synthesized in our lab. PFN was dissolved in methanol (with a few drops of acetic acid to ionize PFN) with a concentration of 1 mg/mL for spin-coating on top of ITO substrate, while PFN was dissolved in CB:DIO (97:3 by volume) solution with a concentration of 25 mg/mL for mixing with PTB7:PCBM[70] active solution. For PTB7:PCBM[70] BHJ active solution, the blending ratio of PTB7:PCBM[70] was 1:1.5 with a concentration of 25 mg/mL in a binary solvent system CB:DIO (97:3 v/v). For PFN:PTB7:PCBM[70] nanocomposite solution (i.e., the PTB7:PCBM[70] BHJ mixture with a small amount of PFN), different weight ratios (0, 1, 3, 5 and 7 wt%) of PFN from CB:DIO solution with a concentration of 25 mg/mL were doped into the PTB7:PCBM[70] active solution, respectively.

Device fabrication: The ITO-coated glass substrates were cleaned by acetone, alkaline lotion, deionized water and isopropanol in order. For the reference two-step coating device with an inverted structure of ITO/PFN/BHJ/MoO$_3$/Al, 10 nm thick PFN layer was firstly spin coated from methanol at 2000 rpm on top of the clean ITO substrate and then 95 nm thick PTB7:PCBM[70] active layer was spin coated on top of the PFN layer. For one-step coating devices with the inverted structure of ITO/PFN:BHJ/MoO$_3$/Al, different weight ratios (0, 1, 3, 5 and 7 wt%) of PFN doping into the PTB7:PCBM[70] BHJ active solution were spin coated directly on top of the clean

Fig. 8 Cross sectional SEM images of (a) Type I and (b) Type II (3 wt%) devices. (SEM bar = 100 nm)

ITO respectively. Finally, 10 nm MoO_3 and 100 nm Al were deposited onto the active layers via thermal evaporation under 3×10^{-4} Pa. The effective area is 14 mm^2 determined by the patterned metal mask. For verifying the effect of the conjugated polymer PFN IML on ITO-free devices, PSCs with the inverted structures of $Al/TiO_x/PFN/BHJ/PEDOT:PSS$ and $Al/TiO_x/PFN:BHJ/PEDOT:PSS$ were also fabricated. 100 nm Al and 4 nm Ti were thermally evaporated onto the glass substrates, respectively, and exposed to air for 12 hours to form the Al/TiO_x cathode. PFN/BHJ bilayer and PFN:BHJ single layer were deposited onto the Al/TiO_x cathode by spin coating. Finally modified PEDOT:PSS (100 nm) was spin-coated on top of the active layer.

Measurements and characterization: The current *J-V* characteristics were measured using a Keithley 2400 source meter under illumination of an AM 1.5G solar simulator with an intensity of 100 mW/cm^2 (Sun 2000 Solar Simulator, Abet Technologies, Inc.). The film thickness was measured by a surface profiler (XP-2). The surface work functions were obtained by SKPFM (SKP 5050, KP Technology). UV-vis absorption spectra were recorded by a Shimadzu UV-2550 UV-vis spectrophotometer. The impedance spectroscopy analysis of capacitance-voltage was investigated by employing a CHI 660D electrochemical workstation. Contact angles using water and formamide as the testing liquid were determined on top of the solid active films using a drop shape analyzer DSA100 instrument. The EQE data were recorded with a QE-R test system from Enli technology company (Taiwan). The film topography was investigated using AFM (Bioscope Catalyst Nanoscope-V). The cross sectional image was measured by SEM (ULTRA55, Zeiss). Highly sensitive EL emission spectra were measured with a Shamrock SR-303i spectrograph from Andor Tech. coupled to a Newton EM-CCD Si array detector. Highly sensitive FTPS spectra were obtained by a Vertex 70 from Bruker optics. Refractive indices of BHJ and PFN:BHJ films were determined by a J.A. Woolam V-VASE spectroscopic ellipsometer in a wavelength range of 300-1000 nm.

Acknowledgements

Notes and references

1 G. Li, R. Zhu and Y. Yang, *Nat. Photonics*, 2012, **6**, 153-161.

2 J. You, L. Dou, K. Yoshimura, T. Kato, K. Ohya, T. Moriarty, K. Emery, C.-C. Chen, J. Gao and G. Li, *Nat. Communications*, 2013, **4**, 1446.

3 Z. He, B. Xiao, F. Liu, H. Wu, Y. Yang, S. Xiao, C. Wang, T. P. Russell and Y. Cao, *Nat. Photonics*, 2015, **9**, 174-179.

4 F. C. Krebs, *Sol. Energy Mater. Sol. Cells*, 2009, **93**, 394-412.

5 F. C. Krebs, *Sol. Energy Mater. Sol. Cells*, 2009, **93**, 1636-1641.

6 F. C. Krebs, *Org. Electron.*, 2009, **10**, 761-768.

7 Y. Liang, Z. Xu, J. Xia, S. T. Tsai, Y. Wu, G. Li, C. Ray and L. Yu, *Adv. Mater.*, 2010, **22**, E135-E138.

8 Y. Liu, C.-C. Chen, Z. Hong, J. Gao, Y. M. Yang, H. Zhou, L. Dou, G. Li and Y. Yang, *Sci. Rep.*, 2013, **3,** 3356.

9 C. C. Chen, W. H. Chang, K. Yoshimura, K. Ohya, J. You, J. Gao, Z. Hong and Y. Yang, *Adv. Mater.*, 2014, **26**, 5670-5677.

10 Z. He, C. Zhong, S. Su, M. Xu, H. Wu and Y. Cao, *Nat. Photonics*, 2012, **6**, 591-595.

11 Y. Yao, J. Hou, Z. Xu, G. Li and Y. Yang, *Adv. Funct. Mater.*, 2008, **18**, 1783-1789.

12 Z. He, C. Zhong, X. Huang, W. Y. Wong, H. Wu, L. Chen, S. Su and Y. Cao, *Adv. Mater.*, 2011, **23**, 4636-4643.

13 S. van Reenen, S. Kouijzer, R. A. Janssen, M. M. Wienk and M. Kemerink, *Adv. Mater. Interfaces*, 2014, **1**, 1400189.

14 F. Zhang, M. Ceder and O. Inganäs, *Adv. Mater.*, 2007, **19**, 1835-1838.

15 Y. Zhou, C. Fuentes-Hernandez, J. Shim, J. Meyer, A. J. Giordano, H. Li, P. Winget, T. Papadopoulos, H. Cheun and J. Kim, *Science*, 2012, **336**, 327-332.

16 Z. Tang, L. M. Andersson, Z. George, K. Vandewal, K. Tvingstedt, P. Heriksson, R. Kroon, M. R. Andersson and O. Inganäs, *Adv. Mater.*, 2012, **24**, 554-558.

17 W. Zhang, Y. Wu, Q. Bao, F. Gao and J. Fang, *Adv. Energy Mater.*, 2014, **4**, 1400359.

18 H. Wu, F. Huang, Y. Mo, W. Yang, D. Wang, J. Peng and Y. Cao, *Adv. Mater.*, 2004, **16**, 1826-1830.

19 F. Huang, H. Wu, D. Wang, W. Yang and Y. Cao, *Chem. Mater.*, 2004, **16**, 708-716.

20 H. Wang, W. Zhang, C. Xu, X. Bi, B. Chen and S. Yang, *ACS Appl. Mater. Interfaces*, 2012, **5**, 26-34.

21 F.C. Chen and S.C. Chien, *J. Mater. Chem.*, 2009, **19**, 6865-6869.

22 S. Yamakawa, K. Tajima and K. Hashimoto, *Org. Electron.*, 2009, **10**, 511-514.

23 J. W. Jung, J. W. Jo and W. H. Jo, *Adv. Mater.*, 2011, **23**, 1782-1787.

24 H. Kang, S. Kee, K. Yu, J. Lee, G. Kim, J. Kim, J. R. Kim, J. Kong and K. Lee, *Adv. Mater.*, 2014, **27**, 1408-1413.

25 P. Fu, L. Huang, W. Yu, D. Yang, G. Liu, L. Zhou, J. Zhang and C. Li, *Nano Energy*, 2015, **13**, 275-282.

26 T. B. Yang, M. Wang, C. H. Duan, X. W. Hu, L. Huang, J. B. Peng, F. Huang and X. Gong, *Energy Environ. Sci.*, 2012, **5**, 8208-8214.

27 Z. Kai, G. Xing, H. Fei and C. Yong, *Acta Chim. Sinica*, 2012, **70**, 2489-2495.

28 D. Ma, M. L. Lv, M. Lei, J. Zhu, H. Q. Wang and X. W. Chen, *ACS nano*, 2014, **8**, 1601-1608.

29 M. L. Lv, M. Lei, J. Zhu, T. Hirai and X. W. Chen, *ACS Appl. Mater. Interfaces*, 2014, **6**, 5844-5851.

30 W. Cai, C. Zhong, C. Duan, Z. Hu, S. Dong, D. Cao, M. Lei, F. Huang and Y. Cao, *Appl. Phys. Lett.*, 2015, **106**, 233302.

31 Q. Wei, T. Nishizawa, K. Tajima and K. Hashimoto, *Adv. Mater.*, 2008, **20**, 2211-2216.

32 K. Yao, L. Chen, X. Chen and Y. Chen, *Chem. Mater.*, 2013, **25**, 897-904.

33 D. K. Owens and R. Wendt, *J. Appl. Polym. Sci.*, 1969, **13**, 1741-1747.

34 K. M. O'Malley, C. Z. Li, H. L. Yip and A. K. Y. Jen, *Adv. Energy Mater.*, 2012, **2**, 82-86.

35 H. Zhou, Y. Zhang, J. Seifter, S. D. Collins, C. Luo, G. C. Bazan, T. Q. Nguyen and A. J. Heeger, *Adv. Mater.*, 2013, **25**, 1646-1652.

36 P. W. Blom, V. D. Mihailetchi, L. J. A. Koster and D. E. Markov, *Adv. Mater.*, 2007, **19**, 1551-1566.

37 K. Harada, A. Werner, M. Pfeiffer, C. Bloom, C. Elliott and K. Leo, *Phys. Rev. Lett.*, 2005, **94**, 036601.

38 M. Vanecek and A. Poruba, *Appl. Phys. Lett.*, 2002, **80**, 719-721.

39 L. Goris, A. Poruba, L. Hod'akova, M. Vaněček, K. Haenen, M. Nesládek, P. Wagner, D. Vanderzande, L. De Schepper and J. Manca, *Appl. Phys. Lett.*, 2006, **88**, 052113.

40 K. Vandewal, K. Tvingstedt, A. Gadisa, O. Inganäs and J. V. Manca, *Nat. Mater.*, 2009, **8**, 904-909.

41 K. Vandewal, K. Tvingstedt, A. Gadisa, O. Inganäs and J. V. Manca, *Phys.Rev. B*, 2010, **81**, 125204.

42 J. Gilot, M. M. Wienk and R. A. Janssen, *Adv. Mater.*, 2010, **22**, 67-71.

TOC
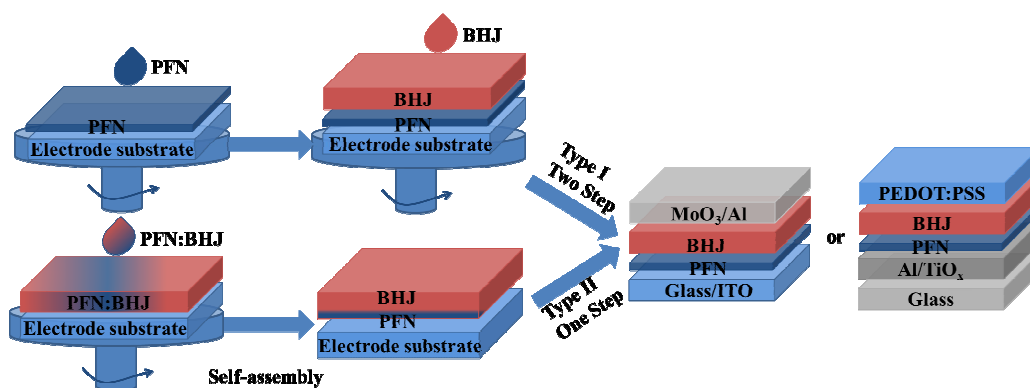
A facile method was reported by blending a conjugated electron-extraction polymer with photoactive materials to simplify the fabrication process.